Mechanical fractionation of tissues using microsecond-long HIFU pulses on a clinical MR-HIFU system

Avinash Eranki, Navid Farr, Ari Partanen, Karun V. Sharma, Christopher T. Rossi, Avi Z. Rosenberg, AeRang Kim, Matthew Oetgen, Haydar Celik, David Woods, Pavel S. Yarmolenko, Peter C.W. Kim & Bradford J. Wood

Taylor & Francis
Taylor & Francis Group

Check for updates

Mechanical fractionation of tissues using microsecond-long HIFU pulses on a clinical MR-HIFU system

Avinash Eranki[a,b], Navid Farr[b], Ari Partanen[b,c], Karun V. Sharma[a], Christopher T. Rossi[d], Avi Z. Rosenberg[e], AeRang Kim[a], Matthew Oetgen[a], Haydar Celik[a,b], David Woods[b], Pavel S. Yarmolenko[a], Peter C.W. Kim[a] and Bradford J. Wood[b]

[a]Sheikh Zayed Institute for Pediatric Surgical Innovation, Children's National Health System, Washington, DC, USA; [b]Center for Interventional Oncology, Radiology and Imaging Sciences, Clinical Center, National Institutes of Health, Bethesda, MD, USA; [c]Clinical Science MR Therapy, Philips, Andover, MA, USA; [d]Department of Pathology, Children's National Health System, Washington, DC, USA; [e]Department of Pathology, Johns Hopkins University, Baltimore, MD, USA

ABSTRACT

Purpose: High intensity focussed ultrasound (HIFU) can non-invasively treat tumours with minimal or no damage to intervening tissues. While continuous-wave HIFU thermally ablates target tissue, the effect of hundreds of microsecond-long pulsed sonications is examined in this work. The objective of this study was to characterise sonication parameter-dependent thermomechanical bioeffects to provide the foundation for future preclinical studies and facilitate clinical translation.

Methods and materials: Acoustic power, number of cycles/pulse, sonication time and pulse repetition frequency (PRF) were varied on a clinical magnetic resonance imaging (MRI)-guided HIFU (MR-HIFU) system. *Ex vivo* porcine liver, kidney and cardiac muscle tissue samples were sonicated (3×3 grid pattern, 1 mm spacing). Temperature, thermal dose and T2 relaxation times were quantified using MRI. Lesions were histologically analysed using H&E and vimentin stains for lesion structure and viability.

Results: Thermomechanical HIFU bioeffects produced distinct types of fractionated tissue lesions: solid/thermal, paste-like and vacuolated. Sonications at 20 or 60 Hz PRF generated substantial tissue damage beyond the focal region, with reduced viability on vimentin staining, whereas H&E staining indicated intact tissue. Same sonication parameters produced dissimilar lesions in different tissue types, while significant differences in temperature, thermal dose and T2 were observed between the parameter sets.

Conclusion: Clinical MR-HIFU system was utilised to generate distinct types of lesions and to produce targeted thermomechanical bioeffects in *ex vivo* tissues. The results guide HIFU research on thermomechanical tissue bioeffects, inform future studies and advice sonication parameter selection for direct tumour ablation or immunomodulation using a clinical MR-HIFU system.

Introduction

Focal or local thermomechanical cancer therapies may play roles in locally dominant disease, pain control, and for antigen presentation or enhanced T-cell maturation in combination with immunotherapy. Local treatment may be delivered with invasive open or laparoscopic surgery, or non-invasive HIFU bio-modulation. Local tumour therapies include surgery [1] or minimally invasive therapies [2] such as radiofrequency (RF) [3,4], cryoablation [5], laser ablation [6,7], microwave ablation [8,9], irreversible electroporation [10,11] and therapeutic ultrasound [12–14]. All local therapies carry iatrogenic risks, but less invasive or non-invasive procedures may carry less risk to nearby critical structures than more invasive options, and may have less pain with quicker recovery [15–18].

In contrast to minimally invasive image-guided therapies, high intensity focussed ultrasound (HIFU) is a non-invasive thermal therapy that precisely focusses acoustic waves on a target tissue (often cancer) within the body, heating the target to over 60 °C and leading to local tissue destruction. HIFU thermal ablation has been used to treat various tumours in multiple anatomic locations including liver, kidney, breast, prostate, uterus, brain and bone [12,14,19–23]. Similar to minimally invasive thermal therapy, HIFU ablation can result in thermal damage to tissues surrounding the treated region due to heat diffusion or off-target heating. This may limit HIFU clinical applicability or efficacy in certain anatomical locations and applications [13,24].

Newer HIFU techniques termed cavitation-cloud histotripsy (CH) [25,26] and boiling histotripsy (BH) [27–29] may overcome certain limitations of HIFU thermal ablation via the mechanical fractionation mechanism, which may have a more distinct and precise margin, with a sharp spatial transition from normal to dead tissue. Unlike HIFU thermal ablation that typically employs continuous wave or high duty cycle ultrasound exposures, these histotripsy approaches

typically apply pulsing regimes at higher acoustic powers and lower duty cycles. In particular, BH uses millisecond-long HIFU bursts, producing shock wave fronts to repeatedly induce boiling at the focus in a short period of time [27,29]. On the contrary, CH uses microsecond-long low duty cycle (<5%) ultrasound pulses to initiate and maintain a dense cavitation bubble cloud [25,26]. Both methods result in mechanical tissue fractionation at the targeted location, likely with variable bioeffects heavily dependent upon the acoustic parameters prescribed.

For both BH and CH, b-mode ultrasound has been used in sonication planning and guidance [28,30], while temperature changes around the focal region were measured using thermocouples [30,31]. However, thermocouples and optical temperature probes are invasive and may not be placed within the focal zone, especially at high acoustic pressures, since they could cause cavitation at the thermocouple tip, resulting in unreliable measurements or probe damage. On the other hand, magnetic resonance imaging (MRI) can be used to accurately and non-invasively plan treatment using T1-weighted and T2-weighted sequences while quantifying relative temperatures in real-time, both within and around the focal region, most commonly using proton resonance frequency shift (PRFS) -based thermometry [29,32–34].

Prior work has explored pulse lengths that are several milliseconds long or in the order of few tens of microseconds [26,27,29]. However, there is a paucity of knowledge on temperature and tissue bioeffects produced by hundreds of microsecond-long HIFU pulses at varying acoustic power, total sonication time or PRF. Additionally, most current research involving these mechanical regimes of HIFU utilise custom-built transducers and systems that may not be well characterised, leading to challenges in standardisation and translation of this HIFU approach to the clinic [30,35]. Systematic exploration of HIFU-mediated thermomechanical bioeffects on a clinical HIFU platform could provide the requisite foundation for future preclinical histotripsy studies. Furthermore, clearer understanding of the sonication parameter-dependent bioeffects at high acoustic pressures using a clinical MR-HIFU system is a requisite to clinical translation of this technology, which may have advantages over existing thermal and mechanical clinical modalities of ablation.

Using a clinical MR-HIFU system to perform sonications with different parameter sets in three types of ex vivo porcine tissue, the objectives of this study were to: (i) characterise resultant lesion types, structure, and viability, (ii) quantify area of temperature and thermal dose at the focal region and (iii) investigate MRI T2 relaxation time -dependent change post-sonication.

Methods and materials

Experiment setup

A clinical MR-HIFU system (Sonalleve V1, Philips, Vantaa, Finland) was used for all experiments. The system is capable of precisely delivering acoustic power with both spatial and temporal control, and consists of a generator cabinet, a patient tabletop with an ultrasound transducer and a therapy
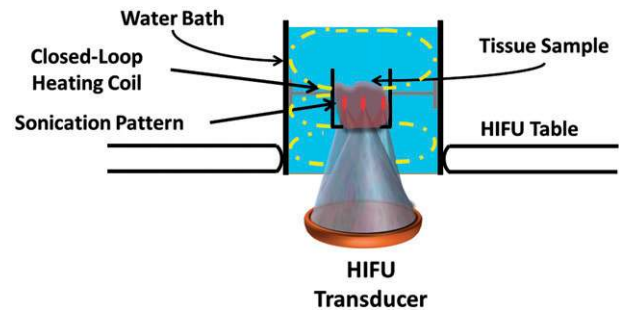
Figure 1. Experimental setup to produce lesions in ex vivo tissues on a clinical MR-HIFU system. The setup consisted of a water bath, filled with degassed water and a closed-loop heating coil that circulated heated water to maintain the water bath temperature at 37.5 °C. A custom-designed tissue holder was positioned at a fixed distance from the transducer. The water bath was placed on the patient tabletop's acoustic window. Each tissue sample (45 mm in thickness) was sonicated using a 3 × 3 grid pattern with 1 mm spacing between foci in either direction.

planning console with control software. The ultrasound array transducer attaches to a positioning system with 5 degrees of freedom, and is submerged in a sealed degassed water tank within the patient tabletop. The spherical shell transducer array consists of 256 elements arranged in a pseudo-random fashion, with a focal length of 120 mm and an F-number of 0.938. The transducer was operated at a frequency of 1.2 MHz, and the acoustic power as well as pulse parameters were controlled using the planning console. The HIFU beam propagates through an acoustic window, producing a focal point of $1.56 \times 1.53 \times 9.37$ mm in size (-6 dB of pressure) [36]. The HIFU system is integrated with a clinical MR imaging system (Achieva 1.5 T, Philips, Best, Netherlands) to perform MRI-based sonication planning and real-time temperature mapping. A passive cavitation detector (PCD) integrated at the middle of the HIFU transducer array was used to monitor for cavitation bubble activity. The centre frequency of this PCD is 650 kHz, which is approximately half of the transmit frequency of 1.2 MHz, with an acquisition rate of 1 sample/500 ms.

The overall setup used for our experiments is depicted in Figure 1. A cylindrical water bath, filled with deionised and degassed water at typical internal body temperature (37.5 °C) and sealed with a Mylar membrane on one end, was placed over the acoustic window. A custom holder to position and fix the tissues within the water bath was designed and 3D printed. The holder consisted of a plastic box with openings at the bottom and top surfaces to permit sonication and exiting beam path (Figure 1). A closed-loop heating system with circulating water was custom built to maintain the tissue temperature at 37.5 °C throughout the experiment. A fresh tissue sample was inserted in the holder for every sonication protocol. An acoustic absorber pad was secured 2 cm from the top of the tissue holder to prevent reflections within the water bath.

Ex vivo tissue preparation

Healthy adult pigs ($n = 3$) were euthanised on an unrelated protocol approved by the Animal Care and Use Committee. Liver, kidney and cardiac muscle tissues were selected since

they represent a broad range of biochemical tissue composition [25,35,37]. All tissue samples were harvested within one hour of animal euthanasia, allowing for greater tissue viability preservation and decomposition control compared to abattoir-obtained tissues. These tissues were immediately cut into multiple, 45 mm thick samples to fit the tissue holder. The prepared tissue samples were transported in a container filled with fresh phosphate buffered saline (PBS, 1×) on ice. This approach may retain cellular function and viability for approximately 72 h [38]. All tissue samples were degassed for two hours in a vacuum desiccant chamber at room temperature while submerged in PBS. Once degassed, the tissues were replaced in the PBS-filled container. Subsequently, the container was placed on ice, and transferred to the MRI suite.

MRI-based sonication planning and monitoring

Relevant details on applied MRI pulse sequences are presented in Table 1. Briefly, a turbo field echo (TFE) survey for localising the tissue sample was performed. Subsequently, a 2D fast field echo (FFE) scan was performed to check for the presence of air bubbles in the ultrasound beam path. A T2-weighted (T2W) 3D turbo spin echo (TSE) imaging sequence was used for sonication planning. MR images for thermometry were acquired in real-time using a multishot RF-spoiled 2D FFE echo-planar-imaging (FFE-EPI) pulse sequence. Temperature and thermal dose maps were calculated online using the PRFS method, and displayed on the therapy planning console. Another set of T2W images with identical acquisition parameters was performed after sonication to visualise the lesion. In addition, quantitative T2 maps were acquired post-sonication using a multi-slice, multi-echo sequence with 5 echo times.

HIFU sonication parameters

Sonication locations were selected on the therapy planning console based on the T2W planning MR images. Locations 25 mm deep within the tissue were targeted in a 3×3 grid pattern with spatial separation of 1 mm between discrete foci (Figure 1). The 1 mm spacing was applied to obtain contiguous fractionated lesions, since 2 mm spacing as typically employed in thermal ablations [32], may result in a gap (i.e., pressures lower than threshold pressure) between foci. To observe effects similar to experiments conducted in vivo, reference temperature for MR-thermometry was set to 37.5 °C, and temperature changes were calculated relative to this baseline temperature. Both the sonication grid pattern and parameter sets (Table 2) were selected to mimic clinically relevant treatment times and volumes, while ensuring safe and consistent operation of the clinical MR-HIFU system. These sonication parameters were selected to coarsely cover ranges that were previously not explored using a clinical MR-HIFU system. Specifically, acoustic power below 500 W did not produce an observable lesion, while powers greater than 800 W risk damage to the transducer. In addition, we selected total sonication times that span wide range of current preclinical and clinical sonications. PRF was chosen to be higher than 8 Hz to compensate for shorter pulse lengths (lesion did not form for PRF below 8 Hz), while, PRF greater than 60 Hz is not feasible on this clinical MR-HIFU system due to hardware limitations. In addition, we calculated total sonication time based on the number of times the 3×3 grid pattern was repeated. For all parameters sets except C and D, the grid pattern was repeated 900 times. For sets C and D, respectively, the grid pattern was sonicated 300 and 1800 times. The entire set of sonication parameters were repeated thrice in liver tissue, while they were performed once in kidney and cardiac muscle tissues.

Histology

Following sonication, tissue samples were trimmed to contain resultant lesions and fixed in 10% neutral buffered formalin for histological processing, which included paraffin embedding and histologic sectioning (5 μm). Subsequently, these tissues were stained with haematoxylin and eosin (H&E) to investigate the structural integrity of tissues, and vimentin

Table 1. List of MRI pulse sequences and their respective parameters applied during histotripsy experiments.

MRI sequence	Type	TR (ms)	TE (ms)	FA (°)	Voxel size (mm)	Slices	FOV (mm)
Survey – target localisation	2D TFE	3.5	1.73	25	$1.47 \times 2 \times 10$	4 axial; 4 sagittal; 4 coronal	200×200
Air bubble detection	2D FFE	150	15	10	$1.25 \times 1.25 \times 2.5$	10 coronal	$280 \times 280 \times 25$
T2w sonication planning	3D TSE	685	35	90	$1.2 \times 1.3 \times 1.5$	50 coronal	$250 \times 250 \times 75$
Real-time MR thermometry	2D FFE-EPI	36	19	20	$2.5 \times 2.5 \times 7$	3 coronal; 1 sagittal	400×310
Post-sonication T2 maps	2D TSE	1200	$20 \sim 105$	90	$1.2 \times 1.2 \times 6$	3 coronal	$80 \times 80 \times 20$

Parameters were held constant for all tissue types and repetitions. TR, TE, FA, and FOV stand for repetition time, echo time, flip angle and field of view, respectively.

Table 2. Sonication parameters used in the experiments for all tissue types.

Parameter set	Acoustic power (W)	Peak positive pressure (MPa)	Peak negative pressure (MPa)	PRF (Hz)	Number of cycles/Pulse	Duty cycle (%)	Total sonication time (s)	Energy (J)
A	800[†]	106.30 ± 1.63	18.38 ± 0.34	10	800	0.66	815.4	4349
B	700	100.97 ± 1.51	18.40 ± 0.55	10	1200[†]	1	818.1	5727
C	700	100.97 ± 1.51	18.40 ± 0.55	10	800	0.66	271.8[†]	1268
D	700	100.97 ± 1.51	18.40 ± 0.55	10	800	0.66	1630.8[†]	7610
E	700	100.97 ± 1.51	18.40 ± 0.55	20[†]	800	1.33	410.4	3830
F	700	100.97 ± 1.51	18.40 ± 0.55	60[†]	800	4	140.4	3931

Acoustic power, pulse repetition frequency, number of cycles/pulse, and total sonication time were varied. Sonication parameters varied are highlighted (†), while others were kept constant. The peak positive and negative pressure values are extracted from Kreider et al. [36].

(Vimentin Bond RTU Primary, Leica Biosystems, IL). Vimentin is an immunohistochemistry marker expressed in most cells of mesenchymal origin, including hepatic stem cell, kidney glomeruli, fibroblasts, endothelial cells and smooth muscle, amongst others. Lack or absence of vimentin staining often indicates significant damage to tissue antigen and viability [39,40]. Briefly, the vimentin staining process involved deparaffinised tissue blocks that were rehydrated and rinsed using deionised water. This was followed by rinsing with peroxide for five minutes. Vimentin antibody was then applied, and tissue was incubated for 10 min. Furthermore, haematoxylin was applied as a counterstain. Finally, tissue was rinsed in peroxide and washed using deionised water. Stained tissues were imaged at 4×, 10× and 40× magnifications (Hamamatsu NanoZoomer-XR, Shizuoka, Japan).

Temperature & thermal dose data analysis

The MRI-based temperature maps were analysed using MATLAB (version R2014a, MathWorks, Natick, MA). All temperature and thermal dose calculations were made within a 71×55 mm region-of-interest (ROI), centred on the focal region. The area of temperature greater than 45 °C at the end of sonication within the coronal and sagittal planes was calculated for all samples. Anything less than 45 °C for these exposure times, was considered milder hyperthermia, generally resulting in no or reversible thermal damage and vascular shutdown compared to higher temperatures (> 45 °C) [41–43]. Cumulative equivalent minutes at 43 °C (CEM43) was used as a metric for thermal dose assessment and was calculated using the following equation:

$$TD(t) = \int_0^t R^{43-T(t)} dt$$

where t is the treatment time and $R = 0.25$ if $T(t) < 43$ °C and 0.5 otherwise [44,45]. Area of thermal dose greater than 240 CEM43 was computed for every sonication in all *ex vivo* samples.

Statistical analysis

All quantitative results are reported as mean ± standard deviation (SD). Comparisons amongst parameter groups in liver tissues were performed using a one-way ANOVA constrained to Bonferroni correction using GraphPad Prism (Version 5.01, GraphPad Software Inc., La Jolla, CA). For all tests, two-tailed p values were obtained, and differences were considered significant if $p < 0.05$.

Results

Effect of sonication parameters on lesion

Appearance and structure
Ex vivo porcine liver was sonicated with each parameter set listed in Table 2. Lesions in all tissue samples were square in shape, resembling the planned sonication. Most sonication parameter sets produced lesions with sharp boundaries between normal and sonicated tissue. Three distinct lesion types were obtained with sonication parameter sets F, A and D, from Table 2. Based on gross pathology, the three lesion types are:

Solid thermal lesions. The solid thermal lesion seen in Figure 2(a2) was created using parameter set F. Even though the total duration of the sonication was relatively short, visual examination of the tissue revealed a white ring around the focal region, suggesting thermal damage. This is supported by the temperature map in Figure 2(a1), showing temperatures greater than 60 °C (instantaneous tissue death) in the entire sonication region. Lack of perfusion further increased thermal effects next to the sonicated region. Gross pathology image of the lesion showed mechanically fractionated centre along with peripheral (apparently thermal) heating effects (Figure 2(a2)). H&E stain revealed hepatic lobules completely disrupted in the middle of the sonicated region, with the edge of the region presenting heterogeneity of completely and partially disrupted hepatic lobules (Figure 2(a3–5)).

Paste-like lesions. Temperature increase in the sonicated region for parameter set A did not extend beyond 50 °C and was contained within the sonicated region (Figure 2(b1)). Figure 2(b2) shows a paste-like lesion with the contents of the lesion in a semisolid state, with nominal structural integrity. Figure 2(b3–5) shows the focal region with partly intact paste-like tissue, along with surrounding intact tissue. The sonicated region contains mostly lysed hepatocytes with few intact hepatocytes. The number of intact cell clusters increase towards the border of this region.

Vacuolated lesions. A vacuolated lesion was obtained using sonication parameter set D, as seen in Figure 2(c2). Although temperature at the sonicated region was not greater than 55 °C, the area of temperature >45 °C was greater than those observed with all other sonication parameters sets (Figure 2(c1)). The centre of the focal region was completely liquefied post sonication. H&E staining revealed intact surrounding tissue, with a central region devoid of tissue structure. Figure 2(c3) shows intact bile ducts less than 800 μm from the focal region. Closer examination of the border of the focal region in Figure 2(c4,c5) shows completely intact tissue with no cell fragments.

Tissue viability post sonication: comparison of H&E and vimentin staining
Immunohistochemical staining for vimentin protein was performed post-sonication in all tissue samples as a surrogate marker for tissue viability (i.e., thermal injury denatures proteins), and compared to H&E stain for tissue integrity and architecture. To illustrate the difference between H&E (Figure 3(a,c)) and vimentin (Figure 3(b,d)), staining, parameter sets C and F in liver tissue are presented. The tissue sonicated with parameter set F displays mechanical tissue fractionation at the focal region that is surrounded by whitening of tissue, an
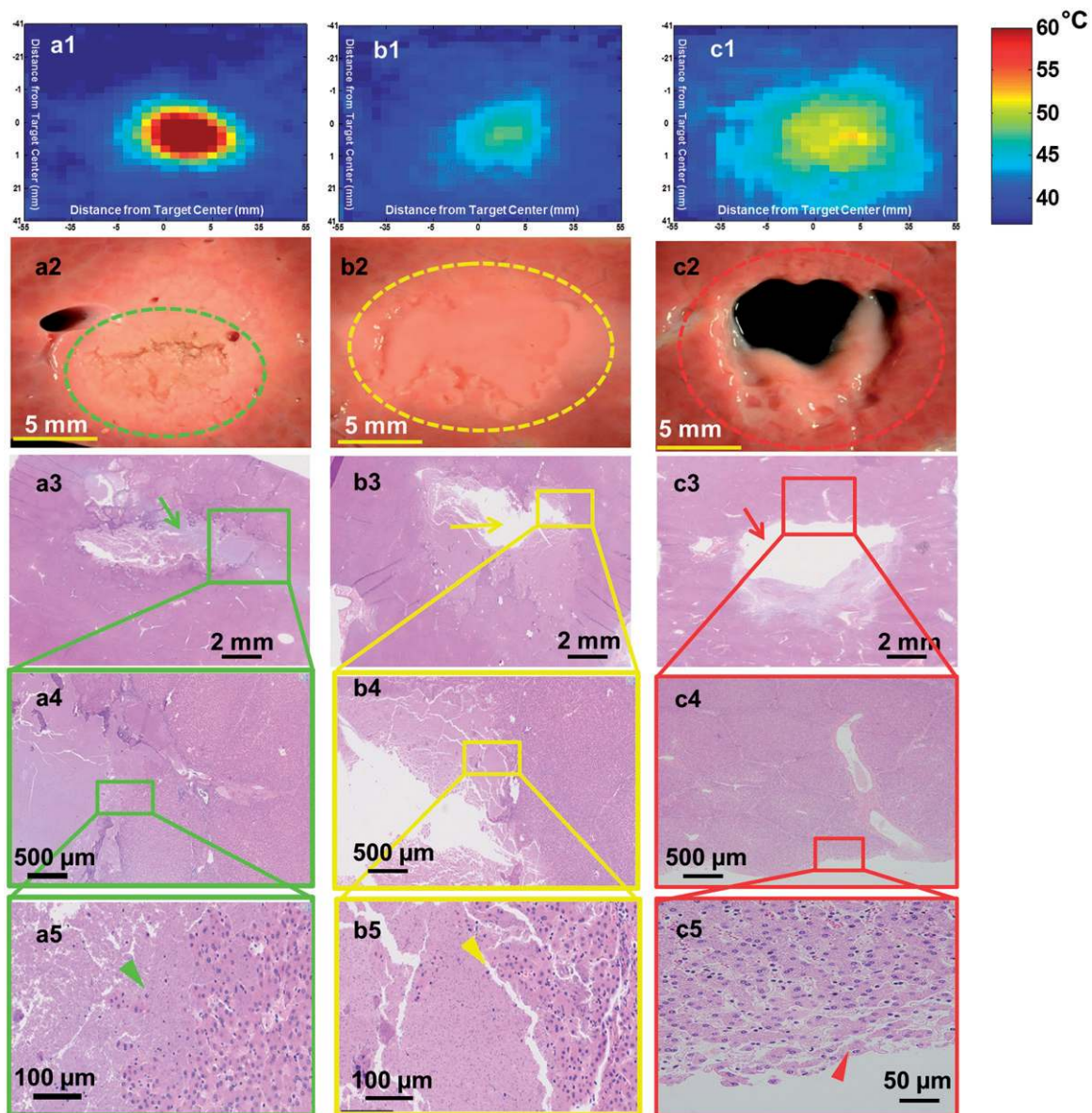
Figure 2. Lesions produced in *ex vivo* porcine liver tissue using sonication parameter sets F, A and D with their corresponding H&E stains are illustrated in a, b & c panels, respectively. These lesions display significantly different morphologies. a1. Thermal map showing temperatures greater than 60 °C in the focal region. a2. Shows a solid thermal lesion (green dotted circle) with mechanical disruption of tissue at the centre of the focal region, surrounded by whitening of tissue. a3. Shows H&E stain with green arrow pointing to the necrosed region of liver. a5. Arrowhead pointing to individual injured cells at the edge of the treatment region. b1. Thermal map displaying temperatures no greater than 50 °C at the focal region, with minimal or no temperature change surrounding this region. b2. Lesion consists of a paste-like tissue in the focal region (yellow dotted lesion) surrounded by a sharp boundary of intact tissue. b3. Shows area of missing tissue in the H&E stain due to loss of the paste during stain process. b4. Region of both intact and necroses tissue. b5. Yellow arrowhead points to hepatic cells partially or completely ruptured. c1. This lesion consisted of the greatest area of temperature, but did not have temperatures increase greater than 55 °C. c2. Displays a vacuolated lesion at the focal region (red dotted circle) with intact tissue around the lesion. c3. Red arrow shows region of vacuolated tissue with intact surrounding tissue. c4&5. Region of intact tissue and vacuolated tissue with red arrowhead pointing to the edge of the lesion that is intact post sonication.

indicator of thermal damage (Figure 3(a,b)). Figure 3(a1) shows H&E stain with partially intact tissue at focal region and intact surrounding tissue (Figure 3(a2,a3)). Figure 3(b) shows vimentin stain within the same region of tissue following sonication with parameter set F. Contrary to the finding with H&E staining, there is a region of intact but presumably injured or non-viable hepatic lobules, inferred from the lack of vimentin staining in Figure 3(b1). Figure 3(b2) shows a region closer to the sonicated region that is injured (yellow arrowhead), with transition region leading to an uninjured hepatic lobule (yellow arrow). It is important to note that although the hepatic lobules appear intact, loss of vimentin

staining may be a surrogate for lack of tissue viability, which may ultimately lead to necrosis.

The right panel in Figure 3 shows another liver tissue sample sonicated with parameter set C. The H&E staining seen in Figure 3(c1) through (c3) show no disrupted hepatic lobules or cells beyond the centre of the focal region, while the centre of the focal region consists mostly of coagulative necrosis of hepatocytes, with a few intact cells. Vimentin staining of this tissue in Figure 3(d) shows normal staining beyond the sonicated region, suggesting no functional damage to immediately adjacent tissue. A closer look at the hepatic lobule at the border of the sonicated region in
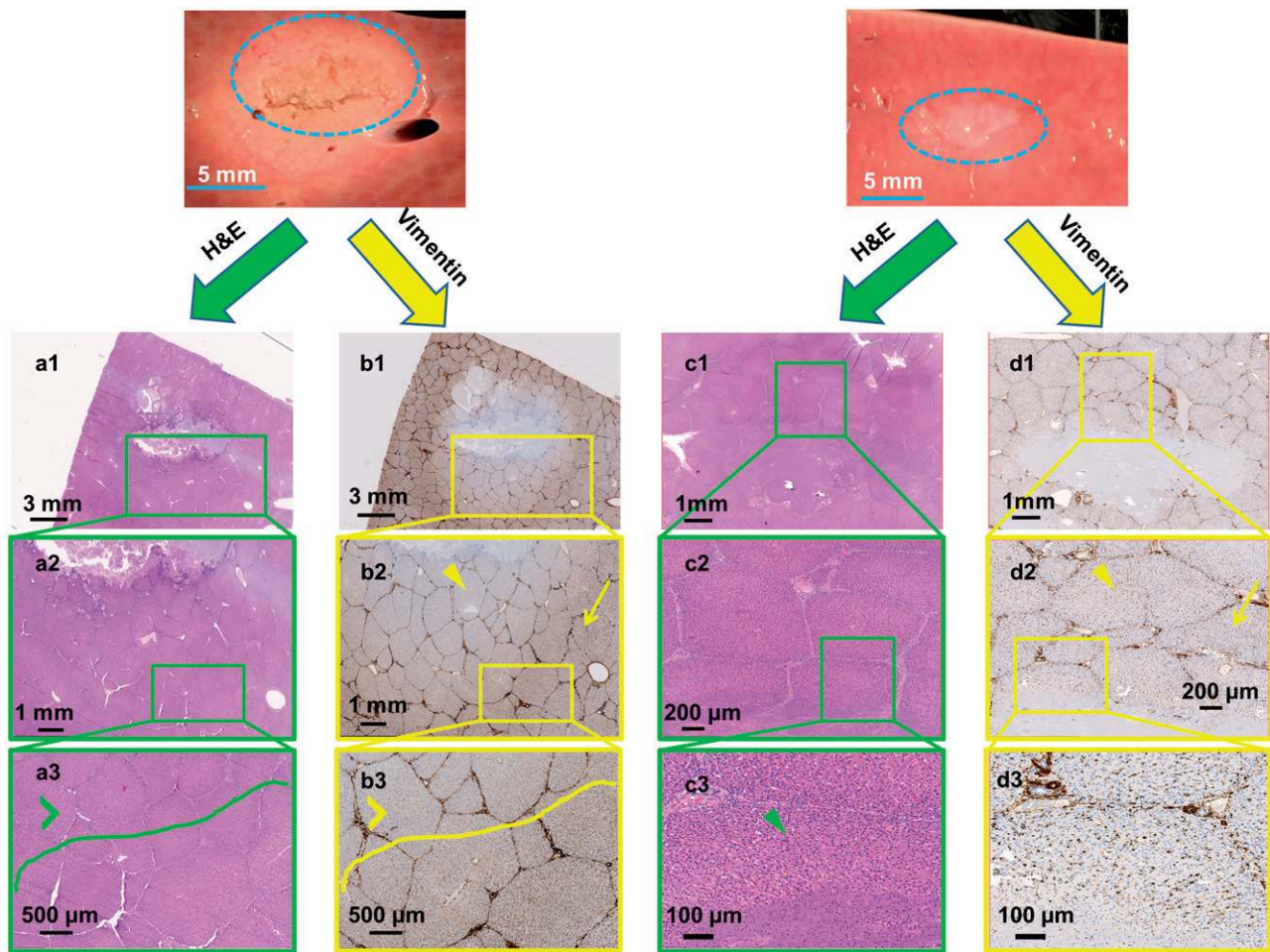
Figure 3. Gross pathology along with H&E and vimentin stains created using sonication parameter sets F (panels a & b) and C (panels c & d). Vimentin stains for mesenchymal cells and is a surrogate for tissue viability. Panel b shows substantial damage of tissue beyond the focal region (panel b2, yellow arrowhead) even though H&E indicates intact tissue (panel a3 green arrowhead). In contrast, panel c shows structurally intact tissue around the focal region and panel d depicts viable tissue in this intact region (green and yellow arrowheads in panels c3 & d2 respectively).

Figure 3(d3) shows partially fractionated hepatic parenchyma, but the rest of the lobule seems to stain normally, suggesting some viability at the cellular level.

Dependence of tissue type on lesion production

Even though all tissue samples had similar thickness, most sonication parameter sets produced dissimilar lesion types in different tissues (Figure 4 is an example for sonication parameter set F). Liver tissue has partial mechanical fractionation along with surrounding thermal bioeffects. On the contrary, kidney tissue had a paste-like lesion with the contents of the lesion appearing fractionated and necrotic. Cardiac muscle tissue displayed a combination of mechanical fractionation and some thermal bioeffects along the boundary of the lesion. H&E staining of the liver tissue shows lysed tissue at the centre of the sonication region with partially disrupted hepatic lobules along the border and several clusters of hepatic cells, some of them with significant cellular injury (Figure 4(a1,a2)). Figure 4(a3) shows several clusters of hepatic cells, with some of them partially ruptured (green arrowhead). The cortex of the kidney was structurally intact post sonication, with the centre of the sonication region containing paste-like cellular contents, seen in Figure 4(b1).

Closer look at the contents at the centre of the sonication region shows mostly lysed cells (yellow arrowhead). The lesion had sharp boundaries with vital proximal structures intact. Cardiac muscle had both mechanical and thermal damage as seen in Figure 4(c). The boundary of the lesion retained its structure, while the centre of the focal region contained liquefied tissue and cellular fragments, seen in Figure 4(c1,c2). Figure 4(c3) shows partially intact cardiac muscle cells (blue arrowhead). Table 3 summarises sonication parameter-dependent lesion types in *ex vivo* porcine liver, kidney and cardiac muscle tissues. All three tissues vary in biochemical composition, density and acoustic attenuation [46], which may explain the variation in lesions obtained using the same sonication parameter set.

Effect of sonication parameters on temperature and thermal dose

Area of temperature >45 °C
The area of temperature greater than 45 °C along the coronal (Figure 5(i)) and sagittal (Figure 5(ii)) planes at the end of sonication was quantified from MR-thermometry data for all sonication parameter sets in liver tissue. Significant differences in this area were found across all sonication parameter
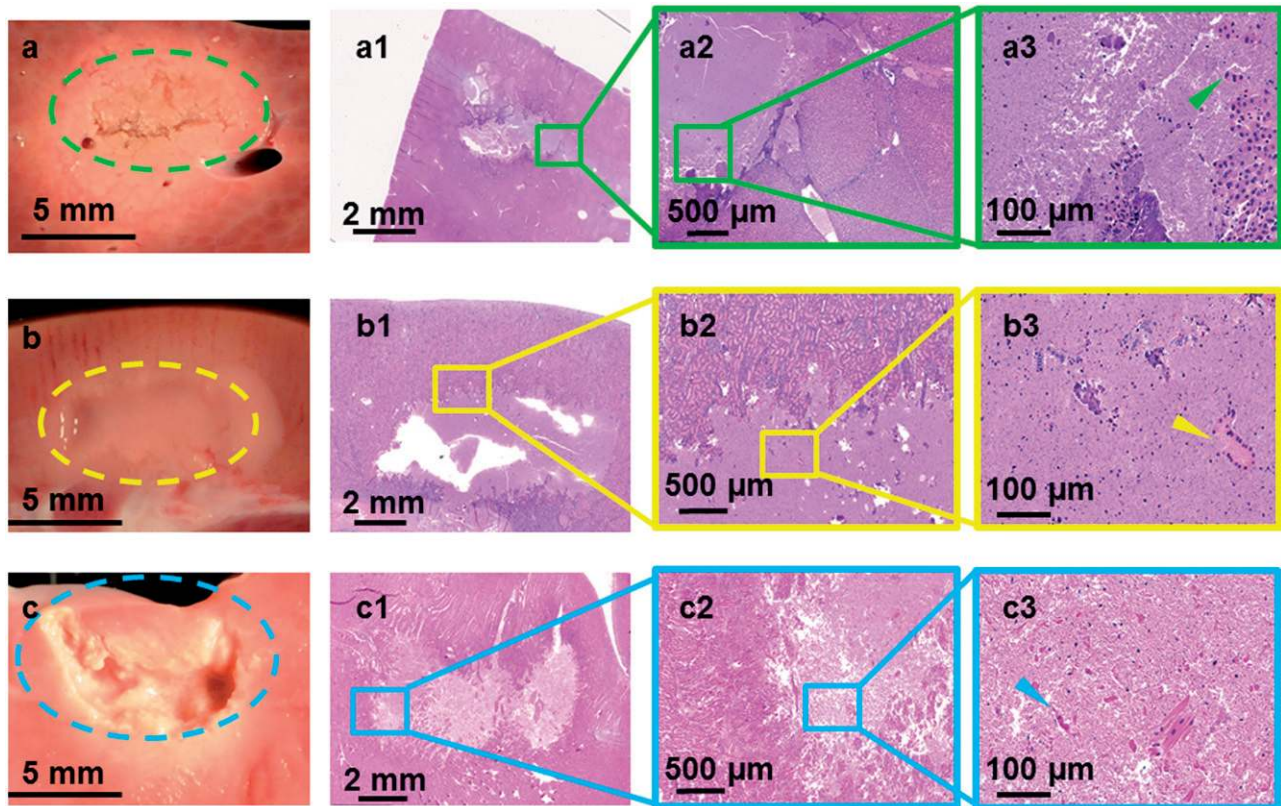
Figure 4. Gross pathology along with H&E stains of lesions produced using sonication parameter set F in porcine liver, kidney, and heart tissues in panels a, b and c, respectively. While the liver tissue expressed solid thermal damage, the kidney presented a paste-like lesion at the focal region. The cardiac muscle showed substantial mechanical fractionation, with some thermal effects along the lesion border.

Table 3. Descriptions of sonication parameter-dependent lesions in *ex vivo* porcine liver, kidney and cardiac muscle tissues.

Parameter set	Liver	Kidney	Cardiac muscle
A	Paste-like	Paste-like	Vacuolated + Mild Thermal
B	Paste-like	Paste-like + Mild Thermal	Vacuolated + Thermal
C	Solid Thermal	Mild Paste-like	Paste-like
D	Vacuolated	Mild Vacuolated	Vacuolated
E	Solid Thermal + Mild Paste-like	Vacuolated	Paste-like
F	Solid Thermal	Paste-like	Mild Vacuolated + Thermal
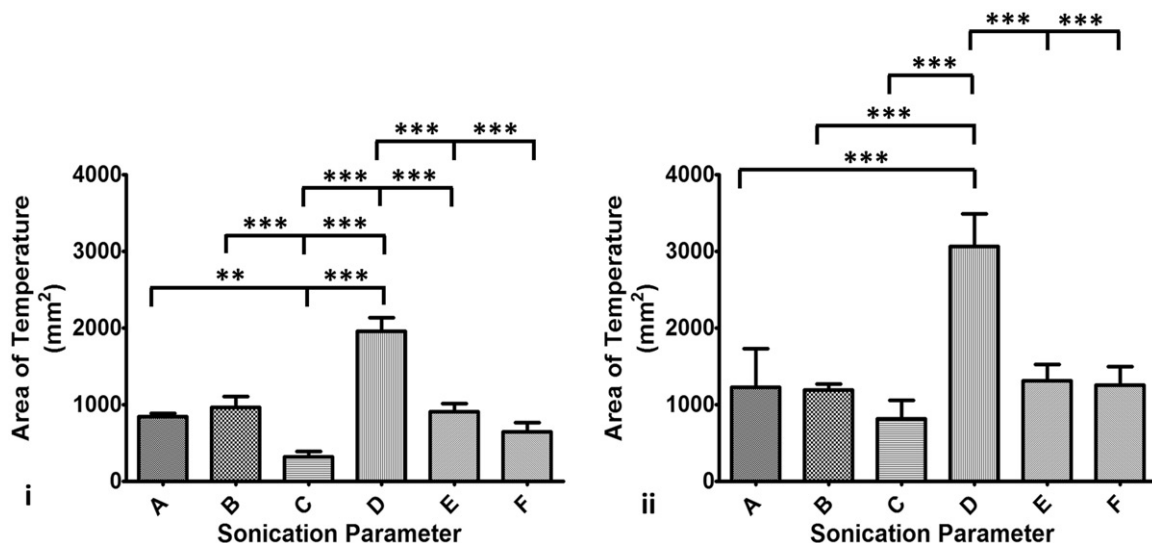
Figure 5. Column chart showing area of temperature greater than 45 °C along the coronal (panel i) and sagittal (panel ii) planes. Statistically different area of temperature was found between D and all other parameter sets, consistent with measurements made along the sagittal plane. Area of temperature was higher along the sagittal plane compared to the coronal plane since the focus region is longer along the sagittal plane than in the coronal plane.

sets in the coronal plane (overall ANOVA $p < 0.0001$). *Post-hoc* test reveals significant differences between parameter set D (1958 ± 173.4 mm^2) and all the other parameter sets ($p < 0.001$, Figure 5(i)). Additionally, significant differences were also found between parameter sets A (841 ± 43.9 mm^2) and C (314.6 ± 76.3 mm^2, $p < 0.01$), parameter sets B (962.5 ± 141.6 mm^2) and C (314.6 ± 76.3 mm^2, $p < 0.001$) and parameter sets C (314.6 ± 76.3 mm^2) and E (645.8 ± 117.3 mm^2, $p < 0.001$). Along the sagittal plane, there was an overall significant difference in area of temperature ($p < 0.001$), with parameter set D (3063 ± 421.9 mm^2) being significantly different from all other parameter sets ($p < 0.001$). However, there was no significant difference in this metric between any other parameter sets (Figure 5(ii)).

Area of thermal dose >240 CEM43

The area of thermal dose >240 CEM43, indicative of lethal tissue damage [42,44], along the coronal plane at the end of sonication was computed from MRI-based thermal dose data for all sonication parameter sets (Figure 6). There was an overall significant difference ($p < 0.0001$) in sampled area that experienced a thermal dose >240CEM43 in this plane. Along the coronal plane, the area of thermal dose for parameter set D (1106 ± 137.5 mm^2) was significantly different from every other sonication parameter set. Furthermore, parameter set B (609.2 ± 313.9) was significantly different from parameter set C (125 ± 59.6 mm^2, $p < 0.05$). Although the area of lethal thermal dose did not change significantly between parameter sets A, B, E and F, lesions produced in liver tissue with these parameter sets were different in type and structure (Figure 6).

Changes in T2 relaxation time and lesion appearance on MRI

Post-sonication, tissue samples were imaged using T2W MRI to assess the degree and type of damage. Lesions appeared as hyperintense regions in T2W images. However, the hyperintense region was less visible in the kidney samples and in samples with higher degree of thermal damage. Post-sonication T2W images of both heart and liver tissues sonicated with parameter sets A and D, respectively, are shown in Figure 7. MRI T2W images visualised the lesions clearly with distinct boundary (and in most samples with distinction between each sonication point), as observed in Figure 7. T2 relaxation times of sonicated and un-sonicated tissue in each sample were calculated (Table 4). Vacuolated and paste-like lesions (parameter sets D and B) produced higher T2 relaxation times compared to thermal lesions (parameter set F). T2 relaxation times inside and outside the lesion were not significantly different in liver tissue between repetitions ($p = 0.5813$ and $p = 0.6978$, respectively). In addition, T2 values were significantly different between within- the lesion and outside -the lesion for all parameter sets ($p = 0.00278$). These preliminary results suggest that a clinical MRI can repeatedly differentiate mechanically fractionated tissues from untreated tissues. This result is valuable but requires
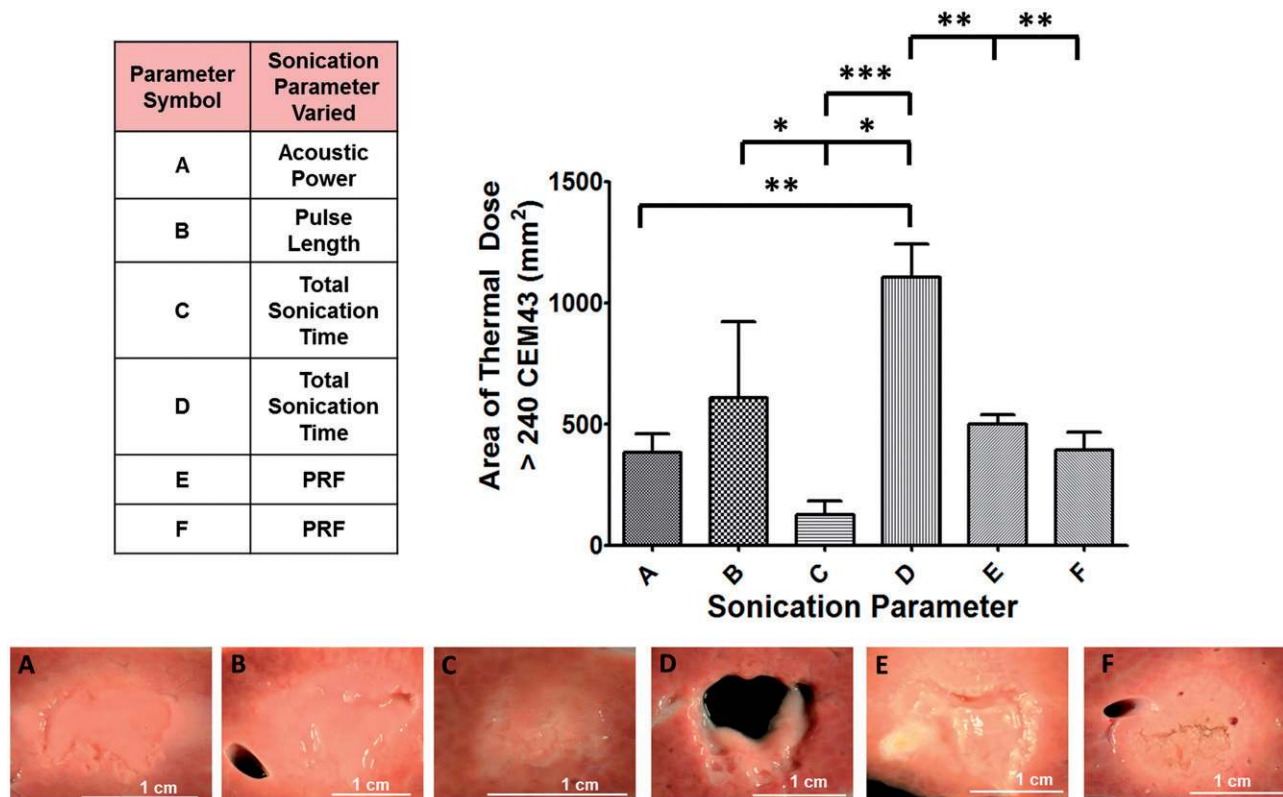
Figure 6. Summary of the varied sonication parameters along with area of lethal thermal dose and corresponding gross pathology images of liver tissue. Area of thermal dose is quantified along the coronal plane and displayed in bar-graph format. Parameter set D was significantly different compared to all other parameter sets. There were additional differences between other sonication parameter sets. Although the area of lethal thermal dose was similar between parameter sets A, B, E and F, the lesions produced were different in structure, as seen in the gross pathology images.
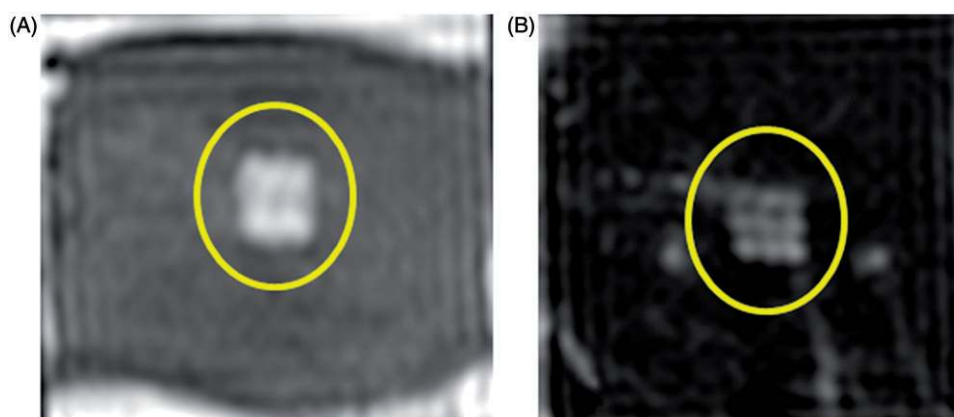
Figure 7. Examples of T2-weighted MR images of *ex vivo* porcine heart and liver obtained post-sonication using parameter sets A (panel A) and D (panel B). The images reveal a square-shaped hyperintense region (yellow circle) consistent with the square sonication grid pattern and with the square fractionated and partially liquefied lesion. Image in panel B also reveals nine spatially distinct points consistent with the sonication grid. (Colored version is available on the journal's webpage).

Table 4. T2 relaxation times inside and outside the sonication region in liver tissue for all sonication parameter sets.

Sonication parameter set	T2 relaxation time inside lesion (ms)	T2 relaxation time outside lesion (ms)
A	84.9 ± 9.9	52.5 ± 4.2
B	92.6 ± 10.9	53.1 ± 3.4
C	64.9 ± 7.6	52.2 ± 3.1
D	123.1 ± 27.2	51.5 ± 2.9
E	58 ± 6.3	50.2 ± 3.1
F	68.4 ± 25.5	49.8 ± 3.8

further optimisation and validation of MRI parameters *in vivo*, before MRI guidance may be relied upon for this task.

Discussion

Bioeffects resulting from hundreds microsecond-long pulsing regimes produced using a clinical MR-HIFU system were investigated in three different *ex vivo* porcine tissue types. Characterization of lesion type and structure relative to achieved temperature is vital in distinguishing and deconvoluting thermal bioeffects from intermingled mechanical bioeffects when utilising micro-second long HIFU pulsing regimes. In order to understand the sonication parameter-dependent bioeffects and lesion characteristics, sonication parameters were modified such as acoustic power, PRF, number of cycles/pulse and total sonication time. In addition, MRI quantified the area of temperature $>45\,^{\circ}$C, area of thermal dose >240 CEM43 and T2 relaxation time.

Herein, we provide observations that can inform the selection of sonication parameters to produce controllable titrateable and predictable bioeffects in liver, kidney, and cardiac muscle on a clinical MRI HIFU system. While liver and kidney have been widely used as target tissues in HIFU research, cardiac muscle was included, since HIFU has potential cardiac-specific clinical applications in, e.g., treatment of arrhythmias, septal defects and hypertrophic obstructive cardiomyopathy [47–50]. Sonication parameters that produce a vacuolated lesion may hold potential in precisely debulking tumours while minimising injury to nearby critical structures (such as nerves) via a sharp, well-demarcated transition zone. On the other hand, sonication parameter sets that produce a paste-like lesion may produce a depot of vital antigens close to vascularised tissue to boost and stimulate a cancer immune response, although this correlation is speculative at present (studies in progress, unreported herein).

The first part of this work focussed on the effect of sonication parameter sets on the resulting lesion types. Some of the sonication parameter sets (e.g., parameter set F) produced predominantly thermal bioeffects along with some mechanical disruption of tissue. This indicates that the rate of heat deposition was greater than that of heat dissipation. The rate of heating for parameter set F was approximately 4.5 to 6.4 times greater compared to all other sets. Additionally, parameter set F had the highest PRF (60 Hz), causing more heat deposition in a short period of time at 700 W. On the other hand, some of these sonication parameters sets produced cell lysate with partially intact cells at the focal region, with little or no thermal damage. For example, parameter set C produced a paste-like fractionated lesion at the focal region with no evidence of thermal damage to surrounding tissue. These results elucidate the ability of certain sonication parameters to limit thermal tissue damage beyond the focal region. Varying pulse length, detailed in parameter set B resulted in paste-like lesion in liver with additional thermal effects in cardiac and kidney tissues. Increasing pulse length enhances resulting thermal effects in tissues due to increased energy deposition and duty cycle. Also, sonication parameters explored in this work show no significant variation in peak negative pressure, but resulting lesion obtained in tissues was different, suggesting the role of PRF, total sonication time and pulse length in lesion production. Table 3 summarises sonication parameter-dependent lesion types in *ex vivo* porcine tissues explored in this study. Same sonication parameter sets produced varying bioeffects in different tissue types. This is due to tissue micro-structure differences causing dissimilarities in ultrasound wave scattering, refraction and attenuation [51]. Specifically, it has been shown that shearing motions of molecules and viscous forces in the media, heat losses due to conduction, and chemical relaxation processes play a strong role in varied ultrasound bioeffects in different tissue types. While tissue bioeffects obtained in this study are similar to previously published work, we wanted to address the bioeffects of unexplored

sonication parameters using a clinical MR-HIFU system [25,35].

We monitored cavitation bubble activity for sonications in all tissue samples. However, due to varying sonications parameters used and limitations with PCD settings (acquisition rate of one sample/500 ms), the cavitation activity may or may not coincide with the actual sonication ON time, and therefore the time of the activity, its duration, or its magnitude is not fully quantifiable with our setup. We are certain, however, that cavitation occurred while using all parameter sets A–F and hypothesise that the mechanical fractionation effects in tissues observed herein were due to cavitation bubble formation in combination with heat caused by incident nonlinear shock fronts. Additionally, cavitation nuclei were shown to appear at 1.2 MHz and at pulse lengths greater than 5 ms [52]. In this work, the intent was to quantify temperature and thermal dose, and to better understand the changes in tissue viability with the proposed sonication protocols. Our data suggest no substantial effect of cavitation activity on temperature measurements. Additional goals included assessment of the ability of a clinical MR-HIFU system to produce clinically relevant and repeatable lesions without any additional non-commercial hardware, making this work applicable across other research institutions. In addition, results reported in this work are repeatable using any calibrated HIFU transducer with an F number $\sim=1$. We demonstrate the potential for such an ultrasound transducer and system with a known power-pressure calibration to produce varying tissue bioeffects with temperature feedback that can be used as a guide for further preclinical and clinical work using similar HIFU transducers and sonication parameters.

Thermal bioeffects were observed on gross pathology images as whitened tissue, while H&E stain showed no definite changes beyond the fractionated tissue boundary. This is in strong agreement with prior work, showing that ablative therapies may cause significant cell death while preserving cellular architecture, or thermal fixation [53]. Additionally, H&E stain is known to be a poor indicator of thermal damage (especially in the acute setting) and shows variable findings from no change to thermal fixation, despite lethal thermal dose shown on cellular viability stains. Furthermore, H&E poorly correlates with cellular outcomes due to ablative therapies [54]. This further warrants the usage of additional stains that provide vital information on cellular viability. For example, nicotinamide adenine dinucloeide-diaphorase (NADH-d) or tetrazolium salts have been shown to stain both viable and unviable tissue regions in ablative therapies [35,55,56]. Depending on the type of lesions produced (semi-solid or liquid), this may result in freeze artefacts or ice crystals. In contrast, vimentin immunohistochemistry does not require freezing tissues post HIFU, thereby avoiding histopathology-related artefacts. Using vimentin stain, significant protein damage surrounding the focal area was seen, with a gradual transitioning to undamaged tissue, a finding attributable to increased heat absorption at higher PRF. Vimentin stain, in future may act as a surrogate marker for cellular and biomolecule viability following HIFU and histotripsy therapies. In the future, it is most informative when

vimentin as well as additional histopathological methods are used to verify sonication parameter -dependent tissue viability beyond the focal region, at different time points post sonication.

Thermoablative techniques such as RFA have repeatedly shown diverse thermal lesion structure based on tissue and tumour type [9]. Our experiments reveal analogous results: the same HIFU sonication parameter set produced vastly dissimilar lesions in different tissues. One potential cause of pronounced thermal damage with sonication parameter set F is that porcine liver tissue has a thin band of interstitial fibrous tissue surrounding each hepatic lobule. This effect is also well pronounced in the heart tissue, possibly due to the dense anatomical structure of the cardiac muscle. These tissue structures may result in significant heat deposition, with little scope for dissipation, leading to enhanced thermal bioeffects. Although all three tissue types exhibited different lesion types, the centre of the focal region was partially lysed. The lysed lesion contents may locally spill cytoplasmic and membrane proteins to blood and lymphatic vessels that deliver antigen-presenting cells or other immunocytes and cytokines. The variable effects of sonication parameters on different tissues may be in part related to tissue elasticity, attenuation, and density. Tissue mechanical fractionation effects may well be optimised to maximise an immune response in terms of antigen presentation without or with less thermal denaturation of the requisite proteins. This ability to titrate bioeffects based upon HIFU parameters could be a powerful tool for the oncologist or immunologist hoping to optimise, calibrate or personalise therapy for a specific tumour type, tissue, or patient.

Sonication-related temperature changes shed light on changes in bioeffects in various tissues. Specifically, we compared area of temperature $>45\,°C$ and area of thermal dose >240 CEM43 for all sonication parameters. Temperature $>45\,°C$ was specifically chosen since it is shown to result in long-term thermal effects including tissue necrosis and vascular shutdown [41,43]. Analysis of both temperature and overall thermal dose allows better understanding and prediction of bioeffects. For example, parameter sets A and C produced similar thermal doses but significantly different temperature profiles in liver. The subsequent lesions were vastly different, with parameter set A producing a paste-like lesion and C causing a thermal lesion. In general, quantification of both area of temperature and lethal thermal doses and its correlation with lesion types and bioeffects could potentially guide selection of parameters for future use.

T2W MRI of the tissue samples was adequate to plan sonications in all three tissue types. Moreover, on post-sonication T2W MRI the HIFU-produced lesions demonstrated higher signal intensity as compared to unsonicated tissue. Tissue fractionation or changes in tissue structure have been shown to produce changes in T2 relaxation time [57,58]. Similar observations were made in our experiments due to tissue structure changes to semi-solid or liquefied debris, causing an increase in T2 signal intensity. These preliminary studies also illustrate the ability of MRI to differentiate fractionated from un-fractionated and thermal lesions. Additionally, T2

relaxation times reported in Table 4 match closely with previously reported values [59,60]. Although in this study the same MR imaging parameters were applied for all tissue types, future studies may optimise these parameters for different tissue types. Finally, additional studies are needed to define a meaningful relationship between T2 relaxation time and the degree of tissue fractionation, liquefaction or thermal damage.

In this work, we used MRI to plan sonications and to quantify temperature as well as cumulative thermal dose in real-time. Although there are limitations in absolute temperature measurements (in terms of scale and location), these limitations in spatial and temporal imaging resolution and sonication pattern were equally distributed for all ultrasound exposure parameters, thus hopefully providing a framework for relative comparison amongst groups. In addition, this approach is applicable when the update time is short compared to the time required for a significant change in temperature during treatment. Also, tissue viability has been reported in vivo to change over a period of time post sonication [53,54]. Therefore, it may be valuable to study the effects of varying tissue viability post sonication using the vimentin stain.

Conclusion

Differing prescriptions for acoustic parameters in this experimental work characterise the resulting lesion types, structure, and viability, tissue temperature and thermal dose, and MRI T2 relaxation times in three types of ex vivo porcine tissues using a clinical MR-HIFU system. These findings are suggestive of mechanisms that may be modulated for non-invasive oncology therapies. Hundreds of microsecond-long HIFU pulses can produce varying lesion types in different tissues, and a clinical MRI system can differentiate the resulting mechanically fractionated from unfractionated regions. This work may inform the selection of sonication parameters to produce controllable thermomechanical bioeffects in liver, kidney and cardiac muscle, and facilitate clinical exploration of this HIFU technique. Successful clinical translation of this technique will depend on assessing the sonication parameter–dependent thermomechanical bioeffects and immune responses in a suitable preclinical in vivo model.

Acknowledgments

Disclosure statement

Dr. Ari Partanen is a paid employee of Philips. Other authors have nothing to declare.

Funding

References

[1] van Doorn RC, Gallee MP, Hart AA, et al. (1994). Resectable retroperitoneal soft tissue sarcomas. The effect of extent of resection and postoperative radiation therapy on local tumor control. Cancer 73:637–42.

[2] Gelet A, Chapelon J, Bouvier R, et al. (2000). Transrectal high-intensity focused ultrasound: minimally invasive therapy of localized prostate cancer. J Endourol 14:519–28.

[3] Dupuy DE, Zagoria RJ, Akerley W, et al. (2000). Percutaneous radiofrequency ablation of malignancies in the lung. AJR Am J Roentgenol 174:57–9.

[4] Gervais DA, McGovern FJ, Wood BJ, et al. (2000). Radio-frequency ablation of renal cell carcinoma: early clinical experience 1. Radiology 217:665–72.

[5] Gill IS, Remer EM, Hasan WA, et al. (2005). Renal cryoablation: outcome at 3 years. J Urol 173:1903–7.

[6] Gangi A, Alizadeh H, Wong L, et al. (2007). Osteoid osteoma: percutaneous laser ablation and follow-up in 114 patients 1. Radiology 242:293–301.

[7] Pacella CM, Bizzarri G, Guglielmi R, et al. (2000). Thyroid tissue: us-guided percutaneous interstitial laser ablation—a feasibility study 1. Radiology 217:673–7.

[8] Wright AS, Lee FT, Jr, Mahvi DM. (2003). Hepatic microwave ablation with multiple antennae results in synergistically larger zones of coagulation necrosis. Ann Surg Oncol 10:275–83.

[9] Brace CL. (2009). Radiofrequency and microwave ablation of the liver, lung, kidney, and bone: what are the differences?. Curr Probl Diagn Radiol 38:135–43.

[10] Davalos RV, Mir L, Rubinsky B. (2005). Tissue ablation with irreversible electroporation. Ann Biomed Eng 33:223–31.

[11] Thomson KR, Cheung W, Ellis SJ, et al. (2011). Investigation of the safety of irreversible electroporation in humans. J Vasc Interv Radiol 22:611–21.

[12] Illing R, Kennedy J, Wu F, et al. (2005). The safety and feasibility of extracorporeal high-intensity focused ultrasound (HIFU) for the treatment of liver and kidney tumours in a Western population. Br J Cancer 93:890–5.

[13] Poissonnier L, Chapelon J-Y, Rouviere O, et al. (2007). Control of prostate cancer by transrectal HIFU in 227 patients. Eur Urol 51:381–7.

[14] Huisman M, Lam MK, Bartels LW, et al. (2014). Feasibility of volumetric MRI-guided high intensity focused ultrasound (MR-HIFU) for painful bone metastases. J Ther Ultrasound 2:b51.

[15] Johnson DB, Solomon SB, Su L-M, et al. (2004). Defining the complications of cryoablation and radio frequency ablation of small renal tumors: a multi-institutional review. J Urol 172:874–7.

[16] Livraghi T, Solbiati L, Meloni MF, et al. (2003). Treatment of focal liver tumors with percutaneous radio-frequency ablation: complications encountered in a multicenter study 1. Radiology 226: 441–51.

[17] Rhim H, Dodd IIIGD, Chintapalli KN, et al. (2004). Radiofrequency Thermal ablation of abdominal tumors: lessons learned from complications 1. Radiographics 24:41–52.

[18] Lawrence VA, Hilsenbeck SG, Mulrow CD, et al. (1995). Incidence and hospital stay for cardiac and pulmonary complications after abdominal surgery. J Gen Intern Med 10:671–8.

[19] Chapman A, Ter Haar G. (2007). Thermal ablation of uterine fibroids using MR-guided focused ultrasound-a truly non-invasive treatment modality. Eur Radiol 17:2505–11.

[20] Kim YS, Keserci B, Partanen A, et al. (2012). Volumetric MR-HIFU ablation of uterine fibroids: role of treatment cell size in the improvement of energy efficiency. Eur J Radiol 81:3652–9.

[21] Chen W, Zhou K. (2005). High-intensity focused ultrasound ablation: a new strategy to manage primary bone tumors. Curr Opin Orthopaed 16:494–500.

[22] Yarmolenko PS, Eranki A, Partanen A, et al. (2018). Technical aspects of osteoid osteoma ablation in children using MR-guided high intensity focussed ultrasound. Int J Hyperthermia 34:49–58.

[23] Sharma KV, Yarmolenko PS, Celik H, et al. (2017). Comparison of noninvasive high-intensity focused ultrasound with radiofrequency ablation of osteoid osteoma. J Pediatrics 190:222–8. e1.

[24] Chaussy C, Thüroff S. (2001). Results and side effects of high-intensity focused ultrasound in localized prostate cancer. J Endourol 15:437–40.

[25] Vlaisavljevich E, Maxwell A, Warnez M, et al. (2014). Histotripsy-induced cavitation cloud initiation thresholds in tissues of different mechanical properties. Ieee Trans Ultrason Ferroelectr Freq Control 61:341–52.

[26] Xu Z, Hall TL, Fowlkes JB, et al. (2007). Effects of acoustic parameters on bubble cloud dynamics in ultrasound tissue erosion (histotripsy). J Acoust Soc Am 122:229–36.

[27] Canney MS, Khokhlova VA, Bessonova OV, et al. (2010). Shock-induced heating and millisecond boiling in gels and tissue due to high intensity focused ultrasound. Ultrasound Med Biol 36:250–67.

[28] Khokhlova TD, Canney MS, Khokhlova VA, et al. (2011). Controlled tissue emulsification produced by high intensity focused ultrasound shock waves and millisecond boiling. J Acoust Soc Am 130:3498–510.

[29] Eranki A, Farr N, Partanen A, et al. (2017). Boiling histotripsy lesion characterization on a clinical magnetic resonance imaging-guided high intensity focused ultrasound system. PloS One 12:e0173867.

[30] Vlaisavljevich E, Kim Y, Allen S, et al. (2013). Image-guided noninvasive ultrasound liver ablation using histotripsy: feasibility study in an in vivo porcine model. Ultrasound Med Biol 39:1398–409.

[31] Kieran K, Hall TL, Parsons JE, et al. (2007). Refining histotripsy: defining the parameter space for the creation of nonthermal lesions with high intensity, pulsed focused ultrasound of the in vitro kidney. J Urol 178:672–6.

[32] Köhler MO, Mougenot C, Quesson B, et al. (2009). Volumetric HIFU ablation under 3D guidance of rapid MRI thermometry. Med Phys 36:3521–35.

[33] Quesson B, Merle M, Köhler MO, et al. (2010). A method for MRI guidance of intercostal high intensity focused ultrasound ablation in the liver. Med Phys 37:2533–40.

[34] Rieke V, Butts Pauly K. (2008). MR thermometry. J Magn Reson Imaging 27:376–90.

[35] Wang Y-N, Khokhlova T, Bailey M, et al. (2013). Histological and biochemical analysis of mechanical and thermal bioeffects in boiling histotripsy lesions induced by high intensity focused ultrasound. Ultrasound Med Biol 39:424–38.

[36] Kreider W, Yuldashev PV, Sapozhnikov O, et al. (2013). Characterization of a multi-element clinical HIFU system using acoustic holography and nonlinear modeling. IEEE Trans Ultrason Ferroelectr Freq Control 60:1683–98.

[37] Häcker A, Chauhan S, Peters K, et al. (2005). Multiple high-intensity focused ultrasound probes for kidney-tissue ablation. J Endourol 19:1036–40.

[38] Lam F, Mavor A, Potts D, et al. (1989). Improved 72-hour renal preservation with phosphate-buffered sucrose. Transplantation 47:767–70.

[39] Battifora H. (1991). Assessment of antigen damage in immunohistochemistry: the vimentin internal control. Am J Clin Pathol 96:669–71.

[40] Hayat MA, Handbook of immunohistochemistry and in situ hybridization of human carcinomas: molecular pathology, colorectal carcinoma, and prostate carcinoma. Vol. 2. London, UK: Academic Press; 2005.

[41] Partanen A, Yarmolenko PS, Viitala A, et al. (2012). Mild hyperthermia with magnetic resonance-guided high-intensity focused ultrasound for applications in drug delivery. Int J Hyperthermia 28:320–36.

[42] Yarmolenko PS, Moon EJ, Landon C, et al. (2011). Thresholds for thermal damage to normal tissues: an update. Int J Hyperthermia 27:320–43.

[43] Gasselhuber A, Dreher MR, Partanen A, et al. (2012). Targeted drug delivery by high intensity focused ultrasound mediated hyperthermia combined with temperature-sensitive liposomes: computational modelling and preliminary in vivo validation. Int J Hyperthermia 28:337–48.

[44] Sapareto SA, Dewey WC. (1984). Thermal dose determination in cancer therapy. Int J Radiat Oncol Biol Phys 10:787–800.

[45] Dewhirst M, Viglianti B, Lora-Michiels M, et al. (2003). Basic principles of thermal dosimetry and thermal thresholds for tissue damage from hyperthermia. Int J Hyperthermia 19:267–94.

[46] Duck FA, Physical properties of tissues: a comprehensive reference book. London, UK: Academic Press; 2013.

[47] Swaminathan A, Rieke V, King RL, et al. (2009). Feasibility of non-invasive 3 T MRI-guided myocardial ablation with high intensity focused ultrasound. J Cardiovasc Magn Reson 11:O86.

[48] Wu Q, Zhou Q, Zhu Q, et al. (2013). Noninvasive cardiac arrhythmia therapy using High-Intensity Focused Ultrasound (HIFU) ablation. Int J Cardiol 166:e28–30.

[49] Yamashita H, Ishii T, Ishiyama A, et al. (2008). Computer-aided delivery of high-intensity focused ultrasound (HIFU) for creation of an atrial septal defect in vivo. Medical Imaging and Augmented Reality 300–10.

[50] Engel DJ, Muratore R, Hirata K, et al. (2006). Myocardial lesion formation using high-intensity focused ultrasound. J Am Soc Echocardiogr 19:932–7.

[51] Luo L, Molnar J, Ding H, et al. (2006). Ultrasound absorption and entropy production in biological tissue: a novel approach to anti-cancer therapy. Diagn Pathol 1:35.

[52] Khokhlova TD, Haider YA, Maxwell AD, et al. (2017). Dependence of boiling histotripsy treatment efficiency on HIFU frequency and focal pressure levels. Ultrasound Med Biol 43:1975–85.

[53] Margulis V, Matsumoto ED, Lindberg G, et al. (2004). Acute histologic effects of temperature-based radiofrequency ablation on renal tumor pathologic interpretation. Urology 64:660–3.

[54] Stern JM, Anderson JK, Lotan Y, et al. (2006). Nicotinamide adenine dinucleotide staining immediately following radio frequency ablation of renal tumors—is a positive stain synonymous with ablative failure?. J Urol 176:1969–72.

[55] Date RS, Biggins J, Paterson I, et al. (2005). Development and validation of an experimental model for the assessment of radiofrequency ablation of pancreatic parenchyma. Pancreas 30:266–71.

[56] Scudamore CH, Lee SI, Patterson EJ, et al. (1999). Radiofrequency ablation followed by resection of malignant liver tumors. Am J Surg 177:411–7.

[57] Allen SP, Hernandez-Garcia L, Cain CA, et al. (2016). MR-based detection of individual histotripsy bubble clouds formed in tissues and phantoms. Magn Reson Med 76:1486–93.

[58] Partanen A, Farr N, Kreider W, et al., editors. Use of MRI to visualize mechanically fractionated lesions generated by boiling histotripsy in tissue. International Symposium for Therapeutic Ultrasound; 2014 April 2-5, 2014; Las Vegas, Nevada, USA.

[59] Hadjisavvas V, Ioannides K, Komodromos M, et al. (2011). Evaluation of the contrast between tissues and thermal lesions in rabbit in vivo produced by high intensity focused ultrasound using fast spin echo MRI sequences. J Biomed Sci Eng 4:51.

[60] De Bazelaire CM, Duhamel GD, Rofsky NM, et al. (2004). MR imaging relaxation times of abdominal and pelvic tissues measured in vivo at 3.0 T: preliminary results. Radiology 230:652–9.